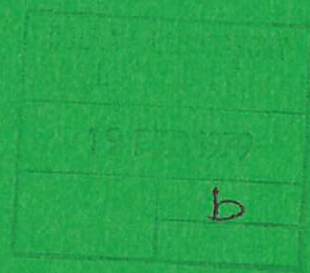




UKAEA

Preprint



LOCAL REGIONS OF HIGH-PRESSURE PLASMA IN A VACUUM SPARK

C R NEGUS
N J PEACOCK

CULHAM LABORATORY
Abingdon Oxfordshire

1979

This document is intended for publication in a journal or at a conference and is made available on the understanding that extracts or references will not be published prior to publication of the original, without the consent of the authors.

Enquiries about copyright and reproduction should be addressed to the Librarian, UKAEA, Culham Laboratory, Abingdon, Oxfordshire, England

LOCAL REGIONS OF HIGH-PRESSURE PLASMA IN A VACUUM SPARK

by

C.R. Negus* and N.J. Peacock
Culham Laboratory, Abingdon, Oxon., OX14, 3DB, UK
(Euratom/UKAEA Fusion Association)

ABSTRACT

The formation of local regions of high-temperature, high-pressure plasma, 'hot-spots', in a vacuum spark is studied using x-ray spectroscopy and holography. Measurements of the dimensions of the hot-spots, of the absolute flux of radiation and of the spectral composition of the x-ray emission, have been analysed to give order-of-magnitude values for the local electron density, temperature, and plasma lifetime. It appears that the plasma pressure is $\geq 10^7$ atmospheres and that the formation of the hot spots requires intense heating rates more commonly associated with focused laser beams, i.e. $\geq 10^{15}$ watts cm^{-3} . It is probable that in the vacuum spark electron beams are responsible for plasma heating. Possible mechanisms for concentrating energy deposition in localised regions are discussed.

(Submitted for publication in J.Phys.D, J.Appl.Phys.)

* on attachment from the University of Leicester

May 1978

CMS

1. INTRODUCTION

Observation of intense x-ray emission from highly-ionised atoms in laboratory plasmas has, almost invariably, indicated the existence of transient, high-pressure plasma regions. In plasmas produced by laser-irradiation of solid surfaces, for example, spectra have been observed from atoms with up to 50 electrons removed. The kinetic pressure, deduced from the parameters in these plasmas (Peacock, 1976) exceeds 1 Megabar. Again, in the plasma focus device (Peacock, 1973) Ar^{+17} ions are produced in a magnetically-constricted plasma whose pressure is somewhat less than 1 Megabar. In electron-beam solid-target experiments at NRL highly-ionised spectra have been reported (Mosher et al 1973). The intensity of the x-ray emission and the neutron emission from deuterated targets are strongly indicative of high-pressure plasma regions where, locally, the electron beam energy is deposited.

In the vacuum spark, with low stored electrical energy, typically ~ 1 kjoule and an apparently simple geometry (Händel 1963, Cohen et al 1968, Lee and Elton 1971, Lee 1974, Schwob and Fraenkel 1972), it is remarkable that ions with even higher ionisation potentials can be produced. These highly - stripped ions appear to be associated with 'hot-spots' which form at the boundary of the plasma layer ablated from the anode by electron bombardment. There are few, if any, convincing measurements of density, temperature or plasma life-time. Even less is known of the mechanism of formation of the 'hot-spot'.

In the present research, parameters of the plasma are deduced from absolute measurements of the x-ray emission and from the intensities of the helium-like resonance lines and their satellites. Also, time-resolved x-ray and holographic studies have been made. These results indicate an energy concentration in the 'hot spots' which is high even for electron beam experiments and is more typical of that produced with focused, high-intensity laser beams. The probability is, however, that in the vacuum spark electron beams are responsible for the energy deposition. Mechanisms for 'focusing' the energy deposition are presented.

2. THE VACUUM SPARK APPARATUS

The vacuum spark apparatus consists of a metal-walled chamber within which are two cylindrical electrodes in vacuo with an inter-electrode spacing of ~ 5 mm. The electrodes are connected via a parallel-plate transmission line to a $19 \mu\text{F}$ capacitor. The circuit inductance, including the chamber and diffuse current channel, is ≈ 40 nH. In order to produce 'hot-spots' the $19 \mu\text{F}$ capacitor was usually operated between 8 and 14 kV. At 12 kV, the calculated peak current is 260 kA. An exploded view of the first source which we have studied is shown in Figure 1. Several electrode configurations were subsequently tried with a view to optimising the regularity of the 'hot-spot' formation.

Much of our earlier studies involved a pointed upper anode as shown in Figure 1. More recently the configuration has been as shown in Figure 2 with a truncated, conical, lower electrode used either as a cathode or anode and a skirted top electrode. The discharge is initiated by irradiating the lower electrode with a 5 joule, 35 nanosecond long pulse from a ruby laser. Irradiation of the electrodes with a focused laser beam replaces the third, trigger electrode more commonly used by other researchers. In all of these electrode configurations 'hot-spot' formation was a common feature of the spatial x-ray emission, see section 4.

The current rose to its peak value in $1.4 \mu\text{sec}$. Discontinuities, presumably due to rapid inductance changes in the plasma start $0.4 \mu\text{secs}$ after the onset of conduction and continue for $1 \mu\text{sec}$. It is during this phase that 'hot-spots' are observed. Thereafter the oscillating current slowly decays with an equivalent resistance of 20 milliohms; there being about five current cycles before cessation of the arc.

3. THE X-RAY SPECTRUM

The x-ray spectrum has been studied with crystal spectrometers. Using a

flat Ge(111) crystal, the spectrum of Figure 3 was produced on Kodirex when exposed to 30 discharges. The electrode configuration was that of Figure 2 with the conical electrode as the anode. The high plasma temperature is indicated by the presence of the Lyman α line of Fe XXVI and the Fe XXV resonance line ($1s^2\ ^1S_0 - 1s\ 2p\ ^1P_1$) at 1.85 Å. The K_α and K_β lines from the anode merge with inner shell transitions in low states of ionisation (i.e. Fe II to Fe XX).

The wavelength resolution of the x-ray spectrum in Figure 3 is determined by the size, or shot to shot variation in the position of the source, rather than the crystal characteristics. The spectral resolution in the Fe XXIV and XXV lines is better than 10^{-2} Å, which corresponds to 'hot-spot' movements from shot to shot of ± 0.1 mm, whereas, if the source were stationary, the crystal rocking curve width (approximately 0.3' for the Ge(III) plane, Evans and Lewis (1977)) would lead to a resolution of 6×10^{-4} Å.

In order to obtain spectra of improved wavelength resolution and to overcome the loss in resolution due to source broadening a curved, focusing, Ge crystal of the Johansson type has been used (i.e. a crystal bent to a radius of $2r$ and the front surface ground to a radius r , where r is the radius of the Rowland circle (R.C.)). Such a crystal, if perfectly made, has the property of Bragg reflecting a point source on the R.C. into a line on the R.C. irrespective of the arc length of the crystal in use. When a point source of x-rays is off-set from the R.C. a finite wavelength range can be reflected while retaining good focusing. Thus the effect of source movement is to extend the wavelength range but without reducing the wavelength resolution. In practice, the resolution is impaired by the standard to which the crystal is ground and bent.

The spectrum integrated over 30 discharges with a Ge 220-plane, Johansson-type crystal is shown in Figure 4. The R.C. radius of 134.6 mm leads to a dispersion of approximately 5×10^{-2} Å/mm. Significant reduction in source broadening is evident in the width of the K_α line relative to that in Figure 3.

TABLE 1

Measured Wavelength (Å)	Identification	Reference
1.759	1.753 Fe I K_{β}	1
1.780	1.777 Fe XXVI Lyman α 1.782 " " " "	5
	1.786 Fe XXV $1s\ 2s\ ^1S_0 - 2s\ 2p\ ^1P_1^o$ $1s\ 2p\ ^3P_2 - 2p\ ^2\ ^1D_2$	
	1.789 Fe XXV $1s\ 2p\ ^3P_1 - 2p\ ^2\ ^3P_2$	
	1.792 Fe XXV $1s\ 2p\ ^1P_1 - 2p\ ^2\ ^1D_2$ $1s\ 2p\ ^3P_2 - 2p\ ^2\ ^3P_2$	
1.850	1.850 Fe XXV $1s^2\ ^1S_0 - 1s\ 2p\ ^1P_1$	4
	Fe XXIV satellites b m n s t w x	3
	1.859 Fe XXV $1s^2\ ^1S_0 - 1s\ 2p\ ^3P_1$	4
1.861	1.865 Fe XXIV $1s^2\ 2s - 1s\ 2s\ 2p$	2
	Fe XXIV a b c d j k l m n q r s t	3
1.863	Fe XXIV j k l q r s t	3
1.906	1.907 Fe XX $1s^2\ 2s^2\ 2p^3 - 1s\ 2s^2\ 2p^4$	2
1.917	1.917 Fe XIX $1s^2\ 2s^2\ 2p^4 - 1s\ 2s^2\ 2p^5$	2
	1.927 Fe XVIII $1s^2\ 2s^2\ 2p^5 - 1s\ 2s^2\ 2p^6$	2
	1.928 Fe XVII $1s^2\ 2s^2\ 2p^5\ 3s - 1s\ 2s^2\ 2p^6\ 3s$	2
1.927	1.930 Fe XVI $1s^2\ 2s^2\ 2p^5\ 3s^2 - 1s\ 2s^2\ 2p^6\ 3s^2$	2
	1.931 Fe XV $1s^2\ 2s^2\ 2p^5\ 3s^2\ 3p - 1s\ 2s^2\ 2p^6\ 3s^2\ 3p$	2
1.937	1.938 Fe I K_{α}	1

1. Bearden, J. A. (1964) X-ray wavelengths. John Hopkins University, Maryland
2. House, L. (1969) Astrophys. Jnl. Suppl. Ser., Vol.18, No.155, 21
3. Gabriel, A. H. (1972) M.N.R.A.S., Vol.160, 99. (Alphabetic notation as introduced by Gabriel).
4. Goltz, E. Ya, et al, (1975) Sov. Physc. Dokl. 20, 49.
5. Kononov, E. Ya, et al, (1977), Fizika Plasmi, Akademik Nauk, USSR, 3, 663-673

The wavelength resolution is improved to $4 \times 10^{-3} \text{ \AA}$ at 1.85 \AA but is a factor of 20-100 times worse, depending on the aperture size used, than would be expected from the rocking curve width of a perfect crystal (Lewis and Evans, 1977). The wavelengths of the lines were calculated by means of the relation

$$\lambda = 2d \sin \frac{1+l_0}{2R}$$

where d is the crystal spacing of 2 \AA and $1+l_0$ is the arc length of the lines from the crystal pole. l_0 , the arc length from the pole to the start of the film, was determined using the helium-like Fe XXV line as a reference.

Additional checks were made on the position of the Fe K_α and Fe K_β lines by using the spark source as a conventional x-ray diode. Listed in Table 1 are the wavelengths and tentative identifications. Again the Fe XXVI Lyman α line has been detected. Suppression of source broadening in the K_α line has permitted observation of K_α -type transitions in highly ionised stages of iron. Improved resolution and increased intensity are needed to identify accurately the components of the multiplets of the lithium-like ion and to determine Doppler broadening. The resonance lines of the dominant ion species e.g. Fe XXV are likely also to be optically thick.

The presence of the Fe XXV emission indicates immediately that the electron temperature is in the keV range. The absolute intensity of the lines and the relative intensity of the satellites form the basis for the spectroscopic analysis leading to average values of the electron temperature and density in the 'hot-spots'.

4. SPATIALLY-RESOLVED X-RAY EMISSION

The x-ray emission has been extensively monitored with pinhole cameras of 0.4 and 2 magnification. X-rays reaching the film traverse a few cm of air and two 0.001" thick mylar windows, one aluminised to exclude visible light. This sets the response of the camera to the wavelength region below 3 \AA as planned. The minute plasma regions or 'hot-spots', which emit intense x-rays, only occur during 1 in about 3 discharges, even though the abrupt current

changes commencing at 0.4 μ s occur regularly.

During the development of the source it was found that with the electrode configuration of Figure 1 intense x-ray emission from the small plasma regions occurred about 1 cm from the cylindrical axis of symmetry of the electrodes, irrespective of the point of laser irradiation. Such spots are shown in Figure 5a, b and c; the latter frame is from the higher magnification (x 2) camera.

In order to produce 'on-axis' spots the source geometry was changed to that of Figure 2. Figure 6 illustrates the types of spatial x-ray emission produced when the conical electrode is used as the cathode. When, however, the conical electrode is used as the anode, the 'hot-spot' is usually produced close to the anode surface, similar to that shown in 5d, but with electrode erosion it can form nearer the cathode with our source.

This work has shown that 'hot-spots' can be formed close to the cathode and off-axis, whereas previous workers (Lee and Elton 1971, Welch and Clothiaux 1974) report spots only near the anode and on-axis. The 'hot-spots' tend to form at the outer boundary, on the cathode side, of a diffuse anode plasma which can extend almost to the cathode itself. It is very evident from the above permutations in electrode configuration, and from the various ways of initiating the discharge, that 'hot-spots' can be produced under a wider range of experimental conditions than has been apparent from the published literature. The 'hot-spots' appear to be something of a naturally occurring phenomenon. Nevertheless, they are not easy to produce consistently in time and space. In order to optimise this aspect of their formation the configuration shown in Figure 2 has proved the most satisfactory.

Two x-ray pin-hole cameras were set up on opposite sides of the vacuum spark in order to observe the same event but through different filters. The object being to discriminate spatially between 'optical' transitions from Fe XXV and screened, K_{α} -type emission. One camera, fitted with a 12 μ m Ni filter transmitted 1.49 to 2 \AA x-rays (i.e. all lines in Table 1

and Figure 4) while the other, fitted with 25 μm Mn transmitted from 1.89 to 2 \AA . This latter camera excludes emission from the highly ionised species of Fe and Fe K_{β} . In the overlapping region (i.e. 1.89 to 2 \AA) both filters transmitted with equal values (the so-called 'Ross filter' arrangement). Frames 7a and c were taken through the Ni filter and the film blackening is due to the total spectral emission shown in Figure 4. Frames 7b and d were taken through the Mn filter and results only from K_{α} type transitions during the same 2 discharges. Analysis of the densitometer traces of Figure 7 show that approximately 85% of the emission from the spot lies in the Fe XXV and Fe XXIV lines near 1.85 \AA and that none of this emission originates in the more diffuse plasma near the anode. Thus, the spot is the source of the very high temperature emission. The remaining 15% of the x-ray emission from the 'hot-spot' is predominately from K_{α} -type transitions in lower ion stages (i.e. \leq Fe XX) as listed in Table 1. These results are in agreement with recent spatially-resolved emission measurements of Feldman et al, (1975) and Kononov et al; (1977).

5. DIMENSIONS OF 'HOT-SPOTS'

The size of the small x-ray emitting region was determined from the umbra projected by the source through a 400 μm pinhole aperture onto the x-ray recording film. The sharpness of the image is in several cases of the order of the grain size in the emulsion. Source dimensions of between 3 and 12 μm have been evaluated from the X2 magnification x-ray camera. An example of this exposure is shown in Figure 5c where magnification of the image has excluded the characteristic x-ray emission from the anode itself.

6. TIME-RESOLVED X-RAY MEASUREMENTS

Evidence has previously been reported (Lee 1974, Cilliers et al 1975, Schwob and Fraenkel 1972), suggesting an exceptionally-long life time for the 'hot-spot', i.e. ~ 10 nanoseconds instead of ~ 20 picoseconds expected for an 'inertial disassembly' time.

Thus time resolved x-ray measurements have been made using a fast PIN

diode (Quantrad) which has a 1.5 nanosecond rise time, 4.5 ns fall time and a 25 mm^2 collecting area. A 0.001 inch thick nickel foil was used to prevent the diode from responding either to scattered laser light or soft x-rays. The diode responded over an energy band from 5 to 25 keV. The diode's output was recorded using a Textronics 605 transient digitizer oscilloscope which has a rise time $< 1 \text{ nsecond}$.

In general, there are two complex x-ray bursts during the first quarter cycle of the discharge. They are separated in time by 400 nanoseconds, Figure 8. The first complex burst was studied in more detail using higher time resolution and with a slit at right angles to the source axis in order to select only those x-rays generated in the inter-electrode region. Fig.9 shows a number of such x-ray bursts, each from different shots. Each single burst lasts for up to 5 ns, when allowance is made for the detector's response time. Taking the detector sensitivity to be 0.8 of its maximum theoretical value of 0.27 amps/watt (Goulding 1966), a pulse duration of 5 nseconds leads to an x-ray emission of 7 to 70 kilowatts in a single burst. The complex x-ray burst occurs more regularly than the highly localised ($\sim 5 \text{ }\mu\text{m}$) x-ray emission shown in x-ray camera pictures. The x-ray burst may be connected with multiple pinching of the plasma column or a plasma instability.

Many ion stages, including the weakly ionised species, could contribute to the apparently single bursts shown in Fig.9, and the only certain way of determining the life-time of the 'hot-spot' is to study Fe XXV or Fe XXVI emission lines. Thus we have incorporated the PIN diode with both the plane- and the Johansson-crystal spectrometer and added an exit slit to select the Fe XXV line at $1.85 \text{ }\text{\AA}$. No consistent time history has been observed for the Fe XXV line owing to lack of efficiency, even when using the Johansson spectrometer at maximum crystal aperture. Figure 10 shows one example of the time history of the Fe XXV line obtained with the Johansson crystal; it indicates an emission time $\leq 1 \text{ nano-second}$, which is shorter than previously reported in the literature, but possibly still longer than the calculated inertial 'confinement' time.

7. ELECTRON TEMPERATURE

The electron temperature and density can be derived from the absolute intensities of the resonance lines $1s^2 1S_0 - 1s 2p^1 P_1$ Fe XXV and $1s^2 S - 2p^2 P$ Fe XXVI. A first approximation is to assume a Maxwellian electron energy distribution and ionisation equilibrium. The line emission using Van Regemorter (1962) rate coefficients and assuming a coronal model is given by

$$\begin{aligned} \frac{dE}{dt} \text{ erg sec}^{-1} &= \int 2.72 \times 10^{-15} \frac{n_e^2}{Z} \cdot q_z \cdot f_{ik} \bar{g} T_e^{-\frac{1}{2}} \cdot 10^{-5040 \psi/T_e} \cdot dV \\ &= \int 2.72 \times 10^{-15} \frac{n_e^2}{Z} \{ q_z \cdot f_{ik} \cdot \bar{g} \cdot G(T_e) \} dV \end{aligned} \quad (1)$$

where q_z is the fractional abundance in charge state Z , see for example, Fig. 11; f_{ik} is the oscillator strength; \bar{g} is the Gaunt factor and ψ (eV) is the excitation energy.

The function $\bar{g} f_{ik} q_z G(T_e)$ is shown in Figure 12 as a function of electron temperature for the resonance lines of Fe XXVI and Fe XXV. Steady state q_z values deduced on steady state balance between ionisation and recombination (Summers 1976) appropriate to $n_e = 10^{21} \text{ cm}^{-3}$ were used. Small contributions from dielectronic recombination into the upper quantum levels have been ignored. Values of q_z are not strongly density dependent and subsequent correction for a more precise density is unnecessary. From the observed intensity ratio of the two lines the effective electron temperature T_e can be deduced:

$$4.3 \text{ keV} \leq T_e \leq 7 \text{ keV}$$

and the above temperature range, corresponding to steady state values, is to be regarded as a range of minimum values.

8(a) ELECTRON DENSITY FROM THE HE-LIKE RESONANCE LINE OF Fe XXV

The x-ray flux F incident on the film of the plane crystal spectrometer during one discharge is related to the radiated energy from the 'hot-spot' during its life-time Δt by

$$\iint F \, dx dy = \frac{dE}{dt} \cdot \frac{\Delta t}{4\pi} \iint R d\theta \, d\phi$$

where x, y refer to rectangular co-ordinates on the film, $\frac{dE}{dt}$ is the peak emission rate as given by equation 1. R is the crystal reflectivity and θ and ϕ are the angles subtended by the reflecting area of the crystal at the 'hot-spot'. For a limited line length on the film, ϕ is approximately independent of θ , y is independent of x and equation 2 reduces to

$$y \int F dx = 2.72 \times 10^{-15} \frac{n_e^2}{Z} q_z \cdot f_{ik} \cdot \bar{g} \cdot G(T_e) \cdot \frac{\Delta V \cdot \Delta t \cdot \phi}{4\pi} \int R d\theta \quad (2)$$

where $\int R d\theta$ is the standard integrated crystal reflectivity which is calculated at 9.6×10^{-5} radians (Evans & Lewis 1977). From section 5 the 'hot-spot' volume is taken to be that of a sphere of radius $5 \mu m$ giving $\Delta V = 4 \times 10^{-10} \text{ cm}^3$. The life-time has been taken as the hydrodynamic disassembly time,

$$\Delta t = \frac{2r}{v_s}$$

where r is the radius and v_s is the sound speed

$$v_s = \left(\frac{ZkT_e + kT_i}{M} \right)^{\frac{1}{2}} = 4.9 \times 10^7 \text{ cm sec}^{-1} \quad (3)$$

Thus

$$\Delta t = 20 \text{ picoseconds}$$

Although there is some experimental evidence, section 6, to suggest Δt may be longer we use the value of 20 psec to calculate density values in this paper. The intensity of the Fe XXV line and equation (2), leads to an electron density in the 'hot-spot' of

$$2.8 \times 10^{21} < n_e < 7.5 \times 10^{21} \text{ cm}^{-3}$$

If now we consider the transient case in which the ion population q_z can be taken as 1 and the excitation rate is increased to its peak value (which occurs when $\log T_e = 8.2$), then we find that the density is reduced by only $1/\sqrt{2}$. A decrease in the assumed lifetime τ would only increase n_e in proportion to $1/\sqrt{\tau}$. Thus the above density values must be substantially correct and only an extended life time, ($\sim 1 \text{ ns}$), could significantly reduce this density range.

8(b) ELECTRON DENSITY FROM THE TOTAL X-RAY EMISSION BELOW 3 Å

The total line emission from an iron plasma has been calculated by Summers (1977) for a range of density and temperature appropriate to the vacuum spark and has been shown to be the major component in the radiation loss. These calculations do not include K_{α}, K_{β} type transitions but the Ross filter experiment showed that such transitions contribute $\leq 15\%$ of the total x-ray output from a hot spot. Comparison of these radiation losses with the intensity registered by the pin-hole camera using calibrated x-ray film has yielded values of the electron density. The electron density has been deduced firstly on the basis of transient ionisation and secondly on the assumption of ionization equilibrium. Table 2 shows the line radiation loss rates firstly for the helium-like iron ions with its fractional population $q(Z=24)$ set to 1 (the transient ionisation case) and, secondly, for ions with charge states $Z=25$ through 22 whose populations are in ionisation-recombination equilibrium.

For steady state ionisation conditions, the average energy incident on the photographic film due to emission from a single 'hot-spot' is

$$E_T = \left(\sum^Z I^Z(\nu) d\nu \right) \Delta V \Delta t$$

We find experimentally that $E_T = 2.48 \times 10^3$ ergs. With $\Delta V = 4 \times 10^{-10} \text{ cm}^{-3}$, and $\Delta t = 2 \times 10^{-11}$ sec the above equation sets $\sum^Z \int I(\nu) d\nu = 3.1 \times 10^{16}$ watts/cm. In order to produce this radiation rate at $T_e \approx 5$ keV (section 8) it follows from the calculations (table 2, column 3) that the electron density is

$$n_e \approx 1.8 \times 10^{22} \text{ cm}^{-3}$$

In fact steady state conditions are just possible at this high density, since the time constant for ionisational equilibrium of helium-like ions is then

$$\tau = \frac{1}{n_e (S_{23} + \alpha_{24})} \approx 5 \times 10^{-12} \text{ sec}$$

In the transient case we assume ionisation dominates over recombination, evidence for which is found from the satellite line intensities in section 9(c).

On this model, formation of the 'hot-spot' is accompanied by rapid burn-through of the low stages of ionisation with the plasma terminating in the helium-like stage from which ion most of the x-ray emission below 3 \AA arises. The total x-ray emission is then

$$E_T = \phi \int I^{Z=24}(\nu) d\nu \Delta V \Delta t \quad (4)$$

where ϕ^{-1} is the fraction of total emission contributed by the Fe XXV. We take $\phi \sim 2$ which is not an unreasonable assumption considering the fractional abundances and loss rates in Table 2.

From equation 4

$$\int I^{Z=24}(\nu) d\nu = 1.5 \times 10^{16} \text{ watts}$$

In the transient model the temperature is more uncertain, however, the temperature must be at least that deduced (section 8) for the steady state, i.e. $T_e > 5 \times 10^7 \text{ K}$. The integral $\int I^{Z=24}(\nu) d\nu$ (table 2, column 2) is not strongly temperature dependent above $5 \times 10^7 \text{ K}$, and for a transient plasma the density would lie in the range

$$8 \times 10^{21} \text{ cm}^{-3} < n_e < 1.3 \times 10^{22} \text{ cm}^{-3}$$

Thus, the electron density deduced from integrated x-ray line emission in steady state or transient ionisation lies in the range $8 \times 10^{21} - 1.8 \times 10^{22} \text{ cm}^{-3}$.

8(c) ELECTRON DENSITY AND $n_e \tau$ VALUES FROM THE HE-LIKE SATELLITE LINES

The relative intensities of the helium resonances lines and their satellites in an iron vacuum spark have been published by Goltz et al (1974), and are remarkably similar to that of Figs. 4 and 5, but with better resolution. These authors have used a quartz crystal Johann spectrograph to cover a smaller wavelength range 0.1 \AA instead of 0.3 \AA as used in the present study. The derivation of the plasma parameters from the relative intensities of the satellites of Goltz has been carried through by Bhalla, Gabriel and Presnyakov (1975). Their analyses show that the equivalent ionisation

TABLE 2

COMPUTED RADIATION LOSSES

$n_e = 10^{22} \text{ cm}^{-3}$ $T_e \text{ K}$	Transient Ionisation, Z=24		Stationary Ionisation	
	$q(Z=24)$	$\int I^Z(\nu) d\nu$ watts cm^{-3}	$q(Z=24)$	$\sum_{z=22}^{z=25} (q_z \int I^z(\nu) d\nu)$ watts cm^{-3}
5×10^8	1	2.03×10^{16}		
2×10^8	1	1.94×10^{16}		
1×10^8	1	1.55×10^{16}	0 .34	8.72×10^{15}
5×10^7	1	8.80×10^{15}	0 .77	9.89×10^{15}
2×10^7	1	1.17×10^{15}	0 .76	8.71×10^{15}
1×10^7	1	3.19×10^{13}	0 .071	1.60×10^{16}
$n_e = 10^{20} \text{ cm}^{-3}$ $T_e \text{ K}$	$q(Z=24)$	$\int I^Z(\nu) d\nu$ watts cm^{-3}	$q(Z=24)$	$\sum_{z=22}^{z=25} (q_z \int I^z(\nu) d\nu)$ watts cm^{-3}
5×10^8	1	2.03×10^{12}		
2×10^8	1	1.94×10^{12}		
1×10^8	1	1.55×10^{12}	0 .41	9.34×10^{11}
5×10^7	1	8.80×10^{11}	0 .75	1.04×10^{12}
2×10^7	1	1.17×10^{11}	0 .38	8.88×10^{11}
1×10^7	1	3.19×10^9	0 .00015	7.71×10^{12}

temperature T_z is lower than the electron temperature $T_e = 2.7 \times 10^7$ K, indicating that the 'hot-spot' is an ionising plasma with non-stationary ion populations.

The population ratio of He-like to Li-like ions, $R = \frac{N_{Z=24}}{N_{Z=23}}$, is given by

$$R \approx \frac{R_s}{1 + R_s \cdot \exp(-n_e t / n_e \tau_s)} \left[1 - \exp(n_e t / n_e \tau_s) \right] \quad (5)$$

where R_s is the relative ion population in the steady state at a temperature T_e . $n_e \tau_s$ is given by the reciprocal of the appropriate ionisation and recombination rate coefficients, i.e. $n_e \tau_s = \frac{1}{\alpha_{Z=24} + S_{Z=23}}$.

For He-like iron in the temperature and density range of interest:

$$8 \times 10^{10} \lesssim n_e \tau_s \lesssim 2 \times 10^{11} \text{ cm}^{-3} \text{ sec.}$$

Inserting the values of R , R_s corresponding to T_z and T_e respectively, the solution of equation (5) yields values for $n_e t$ viz:

$$3 \times 10^{10} \lesssim n_e t \lesssim 5 \times 10^{10}.$$

Again identifying t as the disassembly time for the 'hot-spot' we have

$$1.5 \times 10^{21} \lesssim n_e \lesssim 2.5 \times 10^{21} \text{ cm}^{-3}.$$

The density derived from the satellite line intensities is in fair agreement with that derived from the absolute x-ray flux in the Fe XXV line. A summary of the derived values for the plasma parameters in the 'hot-spot' is given in Table 3.

The assumption of inertial confinement, on which the derivation of density and pressure are based, in fact fits our data rather better than longer confinement times. The product $\langle n_e t \rangle_{\text{abs}}$, derived from the absolute x-ray intensities, scales as \sqrt{t} and, Table 3, is $\langle n_e t \rangle_{\text{abs.}} \approx 3 \langle n_e t \rangle_{\text{sat.}}$; the latter product being derived from the relative satellite intensities, above. Any large increase, say by orders of magnitude, in ' t ' will cause unacceptable divergence in the respective $\langle n_e t \rangle$ values. We should note that an inertial disassembly time for the plasma confinement in the hot-spot is, in theory, not unreasonable. While certain current

configurations have been shown (e.g. Schuurmann et al, (1969) to improve the stability of a pinch, such configurations, if by chance they exist in a vacuum spark, are not likely to prolong stability by more than an order of magnitude over the lowest order instability time used here. An uncertainty in the confinement by an order of magnitude would not greatly alter our analysis or materially affect the conclusions in this paper.

TABLE 3 SUMMARY OF HOT SPOT PARAMETERS

Linear dimensions	5 μm radius
Electron density (from satellite intensities)	$2 \times 10^{21} \text{ cm}^{-3}$
(from absolute radiation flux)	$3 \times 10^{21} \leq n \leq 14 \times 10^{21} \text{ cm}^{-3}$
Electron temperature (steady state)	$4.3 \text{ keV} < T_e < 7 \text{ keV}$
Plasma pressure	$2.7 \times 10^7 \leq n_e k T_e \leq 1.7 \times 10^8 \text{ At.}$
Associated magnetic fields assuming full current flows through 10 μm dia. channel.	$\leq 60 \text{ Megagauss}$
Inertial confinement time	$2 \times 10^{-11} \text{ secs.}$
Radiated x-ray energy ($\lambda < 3\text{\AA}$)	$2.5 \times 10^3 \text{ ergs}$
Radiation loss rate	$\leq 10^{16} \text{ watts cm}^{-3}.$

9. CONSEQUENCES OF NON-THERMAL ELECTRON ENERGIES

A possible source of error in the derivation of n_e and T_e is the assumption of a Maxwellian distribution for the electron velocities. The effect of a two component electron distribution can be seen by considering an extreme case of excitation due to electron impacts from a monoenergetic electron beam. If the mean energy in the beam is equated to that at which the $1s^2 - 1s 2p$ excitation shows a maximum ($\sigma(v)v$ is a maximum at 15 keV), then the energy lost in the 1.85\AA resonance line is given by

$$E(1.85 \text{\AA}) = h\nu \frac{n_e^2}{Z} \sigma(v)v \cdot \Delta V \cdot \Delta t. \quad (6)$$

We calculate that

$$E(1.85 \text{\AA}) \approx \frac{E_T}{12}, = \frac{2.48 \times 10^3}{12} \text{ ergs.}$$

i.e. the intensity of the 1.85\AA line is $1/12$ of the spectrally-integrated emission. Again we take 2×10^{-11} secs for Δt , $4 \times 10^{-10} \text{ cm}^{-3}$ for ΔV , then the electron density (at 15 keV) evaluated from equation (6) is $4 \times 10^{21} \text{ cm}^{-3}$. This is within a factor of 3 of the previous calculations for a $5 \times 10^7 \text{ K}$ thermal distribution. The reason is that at these elevated temperatures the energy distribution is already close to optimum for excitation of the Fe XXV line.

If we now consider another extreme situation, namely that in which the electron temperature is relatively cold and excitation of the ions is due to current-carrying electrons with density n_{ec} in a channel of cross section A, then

$$n_{ec} \approx \frac{2 \cdot 10^5}{A e v_{ec}} \approx 2 \times 10^{21} \text{ cm}^{-3}.$$

Inserting n_{ec} for n_e into equation (6) we find $n_i = \frac{n_e}{Z} = 6 \times 10^{20} \text{ cm}^{-3}$. This is to be compared with $n_i = 1.6 \times 10^{20} \text{ cm}^{-3}$ evaluated for a monoenergetic distribution and $n_i = 4.4 \times 10^{20} \text{ cm}^{-3}$ evaluated from a Maxwellian energy distribution.

Another way of stating these results is that if all the excitation was produced (i) by an electron beam carrying all the current through the 'hot-spot' or (ii) a two-component electron energy distribution or (iii) a Maxwellian distribution of electron energies, then the observed radiation loss would correspond to an electron density covered by the range 3×10^{21} to $1.5 \times 10^{22} \text{ cm}^{-3}$. The main point of note is that whatever the electron energy distribution is in the 'hot-spots', the electron density is consistently high.

10. TIME-RESOLVED HOLOGRAPHIC MEASUREMENTS OF THE ELECTRON DENSITY

The electron density has been determined at various positions in the plasma at non-pinch times by means of two-exposure, microscopic holography. This technique measures the phase change $\phi(xy)$ of a laser pulse in its passage through the plasma and is simply related to the refractive index μ by

$$\phi(xy) = \frac{2\pi}{\lambda} \int_0^L \frac{1-\mu}{\mu} d\ell \doteq \frac{2\pi}{\lambda} \int_0^L \Delta\mu d\ell \quad (7)$$

where ℓ is the path length and (xy) are cartesian co-ordinates perpendicular to $\vec{\ell}$. For the refractive index measurements we must ensure that the laser probe frequency is greater than the other characteristic plasma frequencies such as,

ω_p (plasma frequency), ν (collision frequency) and ω_c (electron cyclotron frequency)

These conditions are satisfied for a ruby laser provided $n_e < 2.3 \times 10^{21} \text{ cm}^{-3}$ and $B_0 < 154 \text{ Mgauss}$. Then, the refractive index takes the simple form

$$\mu = 1 - \frac{\omega_p^2}{2\omega^2} = 1 - \frac{2\pi n_e e^2}{m_e \omega^2} \quad (8)$$

where $\Delta\mu$, equation(7), is $\frac{2\pi n_e e^2}{m_e \omega^2}$

The optical layout for the holography is shown in Figure 13. M2 is a rotatable mirror which is turned, by a spring-loaded hot wire, through a small angle between exposures in order to introduce a reference fringe field. The convex lens ($f = -75 \text{ mm}$) focuses the electrodes onto the hologram. The reference beam passes through two confocal cylindrical lenses and a convex lens to ensure maximum coherence between the scene and reference beam.

The plasma was probed by a ruby laser synchronised with the source-triggering laser and used with variable delays in the range 0 to 10 $\mu\text{seconds}$ in steps of 0.1 μs . The pulse length of the probe laser was clipped down to about 2 nseconds by using half-wave switching of an external KD*P pockel cell, suitably arranged with a polarizer and laser-triggered spark-gap switch.

Some reconstructed holograms are shown in Figure 14. These were recorded with a 5 ns-long probe pulse fired at the times shown relative to the laser which triggered the vacuum spark. Each frame represents a different discharge. The spatial resolution is better than 200 μm which is insufficient to resolve the 'hot-spot'. Initially ($t=0 \mu\text{s}$) only background fringes are present. At $t = 1 \pm .2 \mu\text{s}$ the plasma is radially pinched to a diameter approaching 0.9 mm about 1 mm above the anode, and the background

fringe system is outside the 4 mm field of view. A shift of 7 fringes is clearly evident in the region between 0.45 and 1.55 mm from the axis. Beyond 1.55 mm the electron density is below a value which can readily be estimated corresponding to a fringe shift ≤ 1 . Combining equations (7) and (8) gives

$$\phi(xy) / 2\pi = 3.1 \times 10^{-18} \int_{\ell_1}^{\ell_2} n_e d\ell \quad (9)$$

and setting $\phi(1.55, 0.9) \leq 1$ leads to an electron density of $n \leq 10^{17} \text{ cm}^{-3}$ outside the main plasma column.

With equation (9) and some assumptions regarding the variation of electron density in the region $0.45 < r < 1.55 \text{ mm}$, an estimate of the range of probable peak electron densities at 1 μ second from the initiation of the diode current has been made. Figure 15 illustrates some of the simple models used. On the basis of a linear variation of electron density along the line of sight, the average density within 0.45 mm from the axis of symmetry n_0 (Figure 15) is $1.6 \times 10^{19} \text{ electrons cm}^{-3}$. If, on the other hand, an exponential variation in density along the line of sight ℓ is assumed, i.e. $n = n_1 e^{\alpha \ell}$, then the density n_0 would be in the range 5×10^{19} to $3 \times 10^{20} \text{ cm}^{-3}$, depending on the assumed value of density outside the radius 1.55 mm. This outer density n_1 could lie between 10^{17} cm^{-3} and about $5 \times 10^{10} \text{ cm}^{-3}$; the limits corresponding to a fringe shift of less than unity and the ambient gas pressure at $t = 0$ respectively.

The average central density n_0 at 1 μ s, which is near the time the 'hot-spot' forms, thus lies in the range 1.6×10^{19} to 3×10^{20} . It appears, from the hologram, that this density extends at least 2 mm from the anode surface towards the cathode as shown roughly by the contours in Figure 15. Knowledge of the full extent is limited by the present field of view.

After 1 microsecond, and especially at the later times of 1.9 and 3 microseconds, the reconstructed holograms show dark patches near the anode which could be due to severe refraction or to absorption and reflection of

the laser light by dense and presumably cold plasma. For the case of absorption and reflection the density needs to be close to or exceed the critical electron density, which for ruby light is

$$n_{\text{crit}} = 2.31 \times 10^{21} \text{ electrons cm}^{-3}$$

At other locations fringes are still evident in the holograms at 1.9 and 3.0 μ seconds. The loss in resolution in parts of the holograms may be due to plasma motion during the 5 nanoseconds pulse length of the probe laser. Some shortening of the laser pulse has been tried, but the results are not conclusive.

The general conclusion is that there is a considerable amount of high density plasma (1.6×10^{19} to $3 \times 10^{20} \text{ cm}^{-3}$) present in the electrode gap for extended time periods, and that the spots are formed in this high density plasma.

11. POSSIBLE MECHANISMS FOR ENERGY CONCENTRATION IN 'HOT-SPOTS'

The high radiation loss rates, Table 2, and the spatial singularity of the 'hot-spots' are suggestive of a concentration in energy on a timescale which is not orders of magnitude longer than the inertial disassembly time.

An explanation for the energy concentration which cannot be ruled out at this stage is the explosion of a microparticle of solid material which becomes detached from an electrode and is bombarded by ions or electrons. If we consider heating of the microparticle of volume ΔV by electron bombardment, the energy deposition rate is

$$P_{\text{eb}} = (An_{\text{ec}}) \cdot \bar{v} \cdot \bar{\epsilon} / \Delta V,$$

where \bar{v} is the mean velocity of the electrons with energy $\bar{\epsilon}$, say of 10 keV, which corresponds to the applied voltage and is sufficiently low to be stopped by a 10 μ m diameter particle. The electron current density, n_{ec} , assumed to be

flowing in a vacuum space between the anode plasma and the cathode is given by,

$$I = (An_{ec}) \bar{v} \cdot e$$

With a current of 1.5×10^5 amps and a $5 \mu\text{m}$ radius iron particle, an energy input of 10^{16} watts cm^{-3} can be produced provided the beam has collapsed to a radius of $400 \mu\text{m}$; a plasma constriction of $450 \mu\text{m}$ radius was in fact observed by holography (Section 12). Also, there is evidence of iron dust in the vacuum chamber after a number of shots have been fired. Analysis of dust particles which adhere to the top window shows a preponderance with dimensions $\leq 10 \mu\text{m}$ (Figure 16), and this closely matches the size of 'hot-spots' measured with the x-ray pin-hole camera.

A second explanation which has been promoted by Lee (1974, 1975) and Cilliers et al (1975) is that of electron beam heating in a constricted pinch. This is an attractive suggestion which is in accordance with most of the observations. It does raise some important questions however on the unique character of this particular pinch and the high degree of beam focusing. If most of the diode current is constricted to the 'hot-spot' dimensions magnetic fields of the order of 60 Megagauss are indicated. We then have for the plasma diameter

$$r_p \approx r_{ci},$$

where r_{ci} is the ion cyclotron radius. This is in contrast to conditions which prevail in plasma focus devices, for example, where $r_p \approx (10 \rightarrow 100)r_{ci}$ (Peacock et al 1971). Diffusion of the magnetic fields associated with such a constricted pinch, $\frac{\partial B}{\partial t} = D \frac{\partial^2 B}{\partial r^2}$, is extremely rapid over the 'hot-spot' dimensions with characteristic times even assuming classical resistivity of $\tau_D \sim 1$ nanosecond. During the late stages of the constriction, field penetration might be expected to limit compression heating. Clearly therefore, if compression to $r_p \sim r_{ci}$ is to be explained, anomalous dissipation of the internal magnetic energy must be invoked. Dissipative processes such as for example, current-driven, ion acoustic turbulence could provide the final heat pulse which destroys the confinement.

A third mechanism based on a localised pinch through which the current is carried temporarily (~ 1 ns) by a plasma displacement current can explain the very hard x-rays emission ($\geq 10^2$ keV), Fukai & Clothiaux 1975. The high electric fields of this process would preserve the electron beam character throughout the $10 \mu\text{m}$ spot size. However, the mean free path for ionisation to Fe XXV by 100 keV electrons (if $n_e \sim 10^{20} \text{ cm}^{-3}$) is of the order of 1 cm and would actually inhibit ionisation within the localised pinch dimensions.

One significant difference between the vacuum spark plasma and previously investigated high energy-density pinches is the magnitude of the radiation cooling rate. This leads to a fourth possibility. In recent communications, Shearer (1975, 76) has updated ideas by Pease (1957) and Braginskii (1957) on the equilibria of radiation-cooled pinches. Here the problem can be treated quantitatively and it can be shown that in the presence of highly-charged ions the pinch may shrink isothermally when radiation losses exceed the classical ohmic heat input. The concept, Shearer (1976), is thought to be relevant to observations of singularities in Plasma Focus devices, e.g. Peacock et al (1971), and may also be relevant here. Radiation losses can also provide an energy sink for magnetic energy dissipation in the early stages of the pinch.

Following Shearer (1975), the current, I , in the plasma is given in terms of the Pease-Braginskii current I_{PB} according to

$$I^2 = I_{PB}^2 \frac{P_R}{P_\Omega} \quad (10)$$

where P_R and P_Ω are the radiation loss and ohmic heat input rates. The ohmic heating rate per unit volume is $P_\Omega = \frac{I^2 \eta}{\pi^2 r^4}$ where r is the column radius and η is the classical resistivity.

In the 'hot-spot' plasma with a fraction q_z of the ions in charge state Z , and with resistivity which is anomalously high by a factor F , the limiting current for an equilibrium pinch becomes

$$I'_{PB} = 1.5 \times 10^{-2} \frac{I_{PB} F^{\frac{1}{2}} (kT)^{3/4}}{\bar{Z}^2 \cdot \bar{q}_Z} \quad (11)$$

In equation (11) the main energy losses are bound-bound and free-bound radiation and the functional relation, valid over the range $kT_e > 0.3 Z^2 \text{ Ry}$, given by Galushkin and Kogan (1971) has been used to derive equation (11). For the parameters of our 'hot-spot', Table 3,

$$I'_{PB} = F^{\frac{1}{2}} \times 3.75 \times 10^4 \text{ amps} \quad (12)$$

($Z = 24$, $kT_e \approx 10 \text{ keV}$, $q_z = 1$)

If this current, equation (12), is exceeded the plasma will shrink on a time-scale given by

$$\frac{1}{r} \frac{\partial r}{\partial t} = \frac{P_R}{I^2} \left[\frac{P_{\Omega}}{P_R} - 1 \right] = \frac{3}{4} \frac{1}{\tau_R} \left[\frac{I_{PB}^2}{I^2} - 1 \right] \quad (13)$$

For an iron plasma and $I \gg I_{PB}$, then the shrinkage time is given by

$$\left(\tau_{sh} \right)^{-1} = \frac{3}{4} \frac{1}{\tau_R} \quad (14)$$

where

$$\tau_R = \frac{nkT}{P_R}$$

The shrinkage time, calculated from the computed radiation losses in Table 2, is shown as a function of temperature in Figure 17. The lower the plasma temperature the faster the cooling rate.

As might be expected when the He and H-like lines dominate the spectrum
($10^7 - 10^8$ K)

$$n_e \tau_R = 2 \times 10^{11} \text{ to } 10^{13} \text{ cm}^{-3} \text{ sec, for } 10^{20} < n_e < 10^{22}$$

In Figure 18 we compare values of P_R at various plasma densities with P_Ω ($F = 1$ approximation) at several plasma diameters, both rates being a function of electron temperature. It is evident that at moderately high densities (10^{20} cm^{-3}) and relatively large radii ($r > 100 \text{ } \mu\text{m}$) the radiation losses can exceed the ohmic heat input and the plasma will shrink. Due to this thermal instability, contraction will continue until $P_R \approx P_\Omega$ at $n_e = 10^{22} \text{ cm}^{-3}$ and $r = 10 \text{ } \mu\text{m}$. These plasma parameters are very close to those measured for the 'hot-spot'. Furthermore the holographic results indicate that the initial plasma density and size ($n_e \geq 2 \times 10^{19}$, $r \approx 450 \text{ } \mu\text{m}$) are suitable for onset of radiation induced shrinkage. Any local density enhancement would increase P_R and enhance the effect. It is possible that an iron particle explosion might even be the precursor to a radiation cooled pinch. It should be noted that most of the shrinkage takes place at densities less than the peak value and it is therefore a relatively slow process, i.e.,

$$n_e \tau_{\text{conf}} \lesssim n_e \tau_{\text{sh}} \sim n_e \tau_R$$

Thermal conduction losses from the ends of the shrinking column could be comparable, or even higher, than the radiation loss.

The main characteristics of the 'hot-spot' could therefore be explained qualitatively by space-charge neutralisation of the electron beam in the anode plasma followed by a radiation and current induced ($I > I_{PB}$) shrinkage of the pinch. At the high current density associated with the 'hot-spot' the electron drift velocity much exceeds the ion-acoustic velocity and can even approach the electron thermal velocity. Under these circumstances an explosive deposition of beam energy can be anticipated. The detailed physical processes involved in this absorption are only as yet speculative.

12. CONCLUSIONS AND SUMMARY

Order of magnitude values for the plasma parameters in the 'hot-spots' formed in a vacuum diode have been derived from a spectroscopic analysis of the x-ray emission. Concentrations of energy in the 'hot-spots' are typical of those more commonly associated with focused high-power laser beams.

Mechanisms for the energy concentration have been suggested and involve local deposition of energy from electron beams in the diode. Formation of the 'hot-spot' may be due to a thermal instability in the beam, induced perhaps by shrinkage of the plasma column due to radiation cooling. Explosion of a micro-particle may also be a mechanism contributing to the localisation of the initial plasma in the diode gap. In order to evaluate the physics of the 'hot-spot' formation with greater certainty several key measurements are indicated. These include the density-time evolution during the 'hot-spot' formation, the magnetic fields associated with the current in the 'hot-spots', and very much better time resolution than has heretofore been available.

ACKNOWLEDGEMENTS

This project was supported by the U.S. Air Force Office of Scientific Research under grants AFOSR - 73 - 2519 and AFOSR - 76 - 3060.

The authors would like to acknowledge the benefit derived from discussions with their colleagues, in particular D.E.T.F. Ashby, Culham Laboratory, and J. D. Lawson, Rutherford Laboratory, on electron beams. They are indebted to H. Summers (University of Cambridge) for his calculations of the ion abundances and radiation rates for an iron plasma.

REFERENCES

- Bhalla C P, Gabriel A H and Presnyakov L P (1975) Mon.Not.Roy.Ast.Soc., 172, 359
- Braginskii S I (1957) Zh.Eksp.Teor.Fiz. 33, 645
- Cohan L, Feldman U, Swartz M and Underwood J H (1968) J.Opt.Soc.Am., 58, 843
- Cilliers W A, Datla R U, and Griem H R (1975) Phys. Rev. A12, 1408
- Evans K and Lewis M (1977) Private Communication, University of Leicester
- Feldman U, Goldsmith S, Schwob J L, Doschek G A (1975) Astrophys.J. 201, 225
- Fukai J and Clothiaux E J, (1975) Phys.Rev.Lett. 34, 863
- Goltz, E Ya, Zhitnik I A, Konov E Ya, Mandelshtam S L and Sideelnikov Yu V (1975) Soviet Physics, Doklady 20, 49
- Galushkin, Yu I, Kogan, V I, (1971) Nuclear Fusion 11, 597 - 604
- Goulding F S (1966) Nucl.Instr.Meth. 43, 1
- Handel S K (1963) Brit.J.Appl.Phys. 14, 181 - 185
- Klapisch M, Schwob J L, Fraenkel B S and Oreg S (1977) J.Opt.Soc.Am., 67, 148
- Kononov E Ya, Kotselev K N, Sidelnikov U V (1977) Akad.Nauk. USSR Fisika Plasmi 3, 663
- Lee T N and Elton R C (1971) Phys.Rev. A3, 865
- Lee T N (1974) Astrophys.J., 190, 467
- Lee T N (1965) Annals of N.Y. Acad. 251, 112
- Mosher, D, Stephanakis, S J, Vitovitsky, I M, Dozier, C M, Levine, L S and Nagel, D J (1973) Appl.Phys.Lett., 23, 429-430
- Peacock N J, Hobby M G and Morgan P D. Proc 4th Conf. on Plasma Physics and Controlled Nuclear Fusion Res., Madison, USA (1971) CN-28/D-3, pp 537-551
- Peacock N J (1973) Kirtland Air Force Weapons Lab. report, AFWL-TR-73-147, New Mexico, USA
- Peacock N J (1976) Beam-Foil Spectroscopy, 2, 925, Plenum Press, New York
- Pease R S (1957) Proc.Phys.Soc. B 70, 11
- Quantrad Corp. PIN diode 025-PIN-250, Los Angeles
- Schwob J L and Fraenkel B S, Phys.Lett. (1972) 40.A.1, 81-85
- Shearer J M (1975) Lawrence Livermore Laboratory Report UCID-16973
- Shearer J M (1976) Physics of Fluids, Vol.19, No.9, 1426-1428
- Schuurman W, Bobeldijk, C, De Vries, R F (1969) Plasma Physics 11, 495-506
- Summers H (1977) Mon.Not.R.Astr.Soc. 178, 101 (the present calculations represent an extension of this model to plasma conditions appropriate to the vacuum spark plasma).
- Van Regemorter H (1962) Astrophys.J. 136, 906
- Welch T J and Clothiaux, E J (1974) J.App.Phys. 45, 3825 -3827

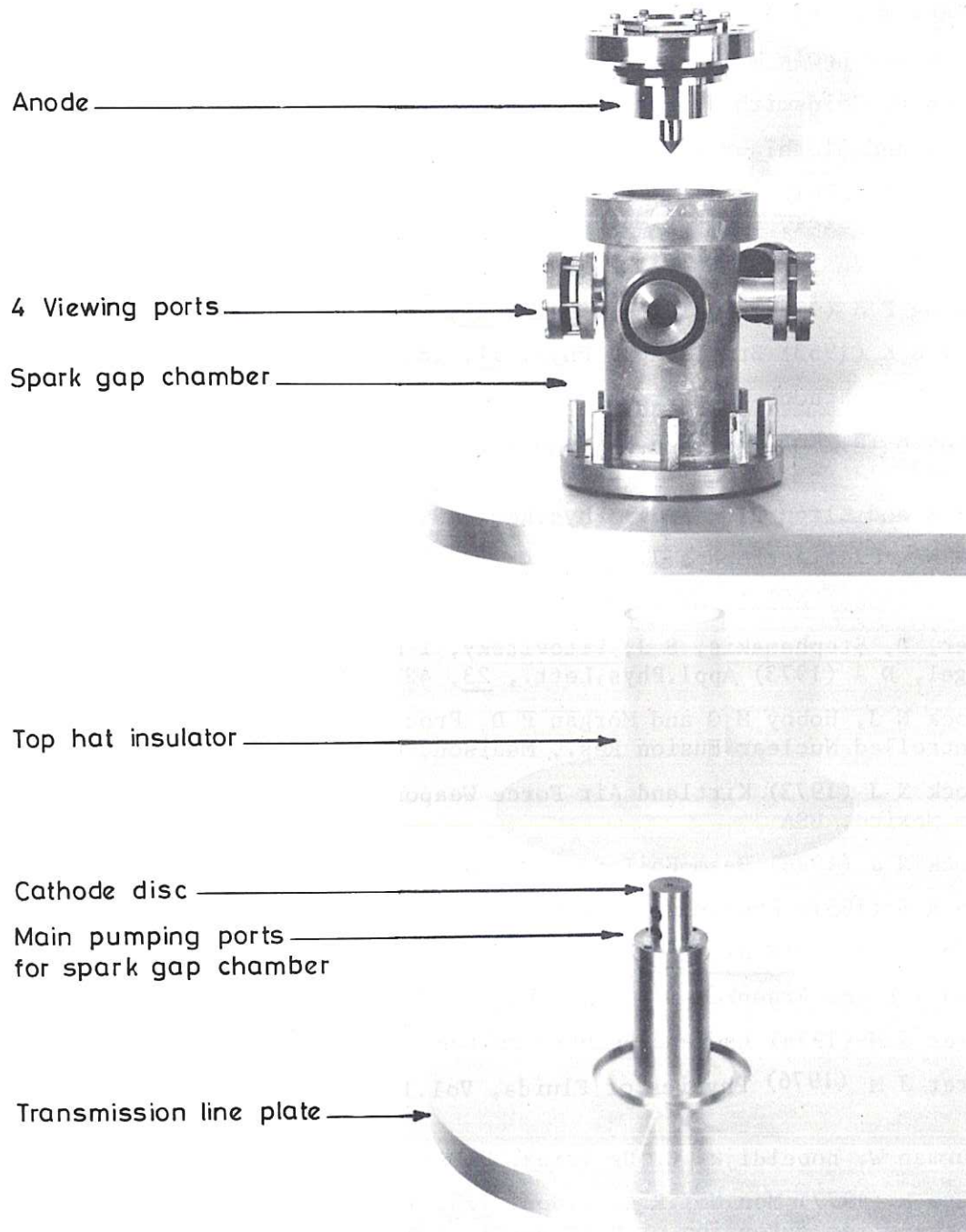


Fig.1 Exploded view of the spark source with the early electrode geometry. This produced off-axis 'hot-spots' near the cathode surface. The laser beam entered the chamber through the anode at an angle to the axis of symmetry.

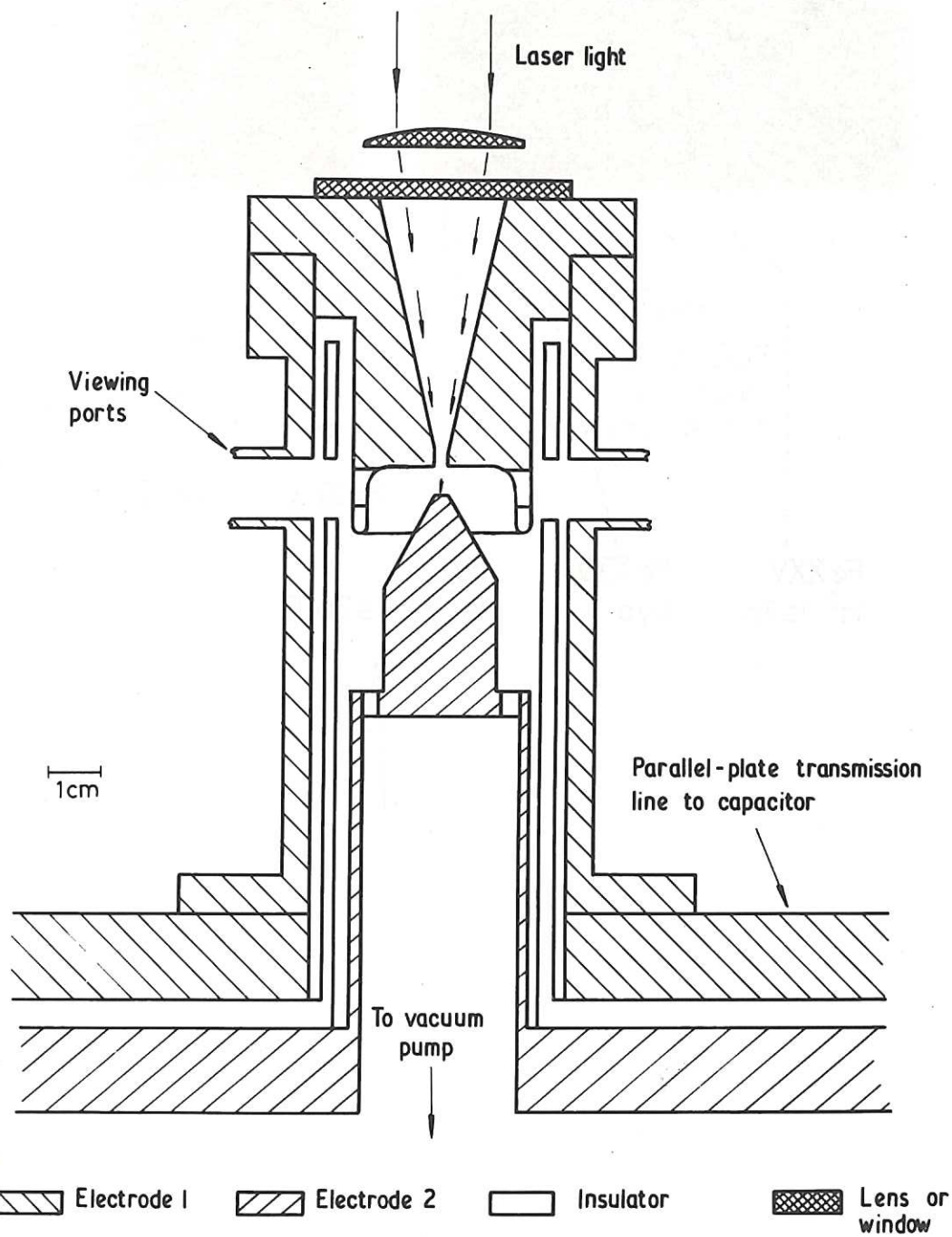


Fig.2 Schematic drawing of the source approximately 0.8 full scale used for producing on-axis 'hot-spots'.

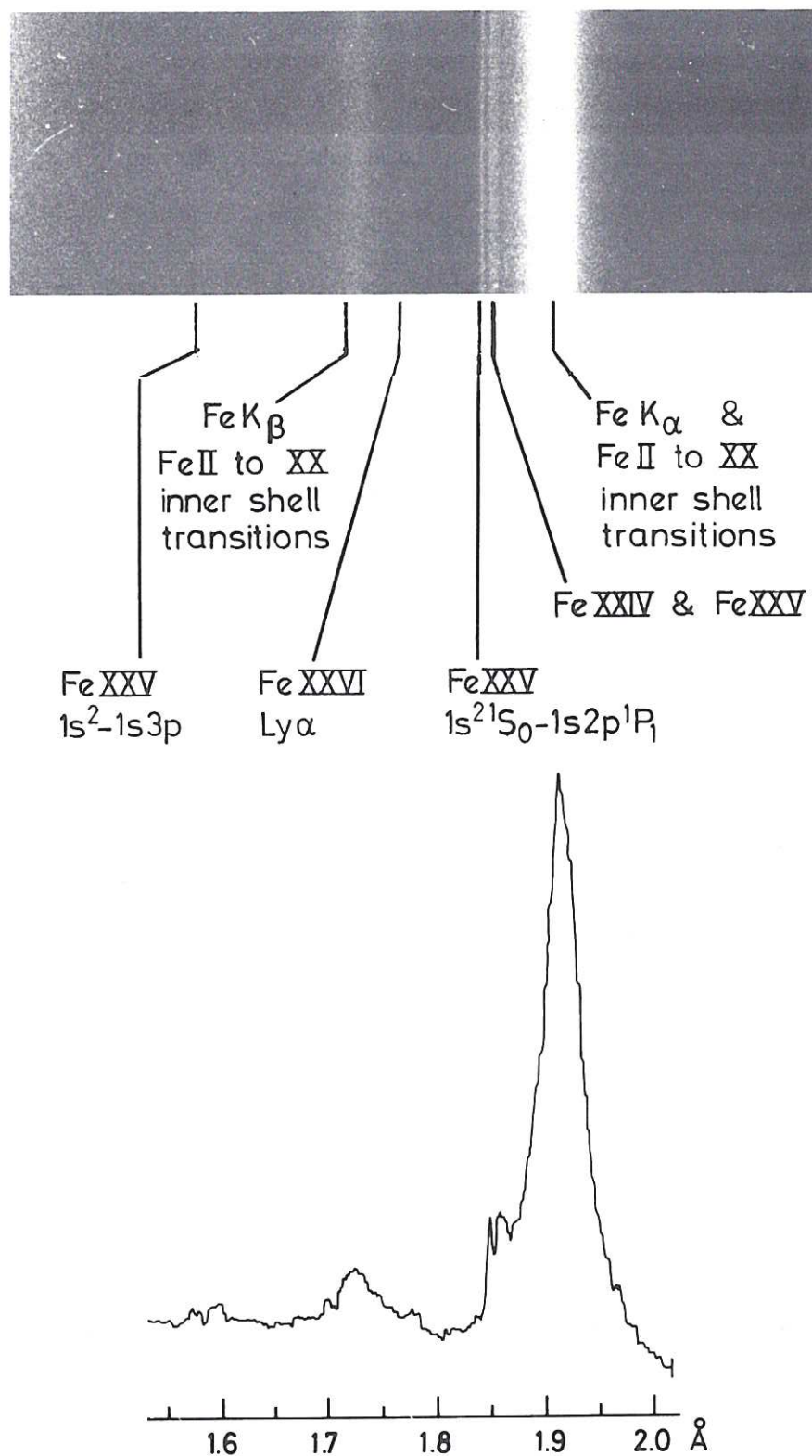


Fig.3 X-ray spectrum obtained with 30 shots using a plane germanium crystal spectrometer. The source configuration was as shown in Fig.2 with the lower electrode as the anode.

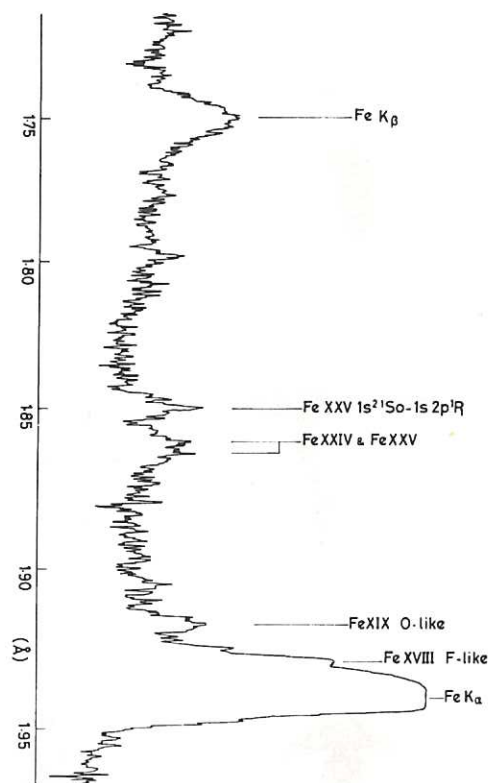


Fig.4 X-ray spectrum obtained with 30 shots using a curved germanium crystal spectrometer of the Johansson type. The source configuration was as shown in Fig.2 with the lower electrode as the anode.

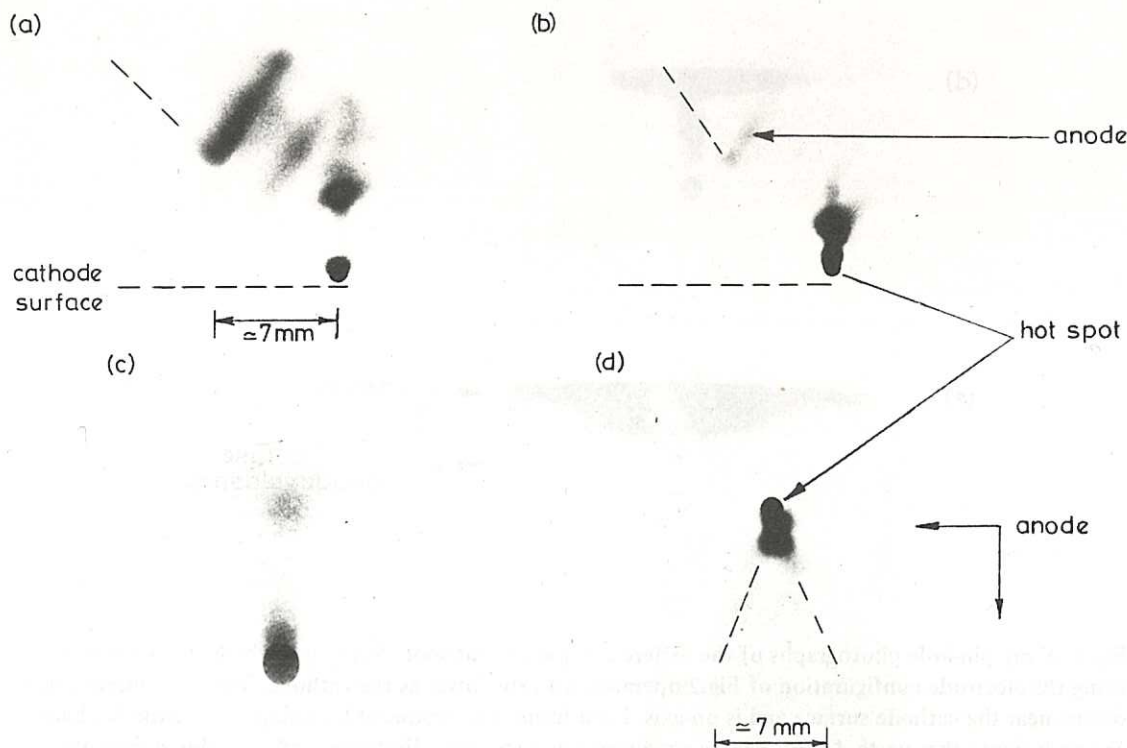


Fig.5 X-ray pin-hole photographs of the anode and 'hot-spot' in the wave-length region below 3 Å. Frames a, b, c show off-axis, near-cathode 'hot-spots' produced using the source configuration in Fig.1. Frame c was obtained with an x-ray camera of higher magnification ($\times 2$) than used for the others and the anode is not visible; such negatives have been used to determine the size of the 'hot-spots' from the extent of the umbra. The width of the umbra is not discernable in these figures due to their limited magnification. Frame d shows the more common 'hot-spot' which is formed close to the anode.

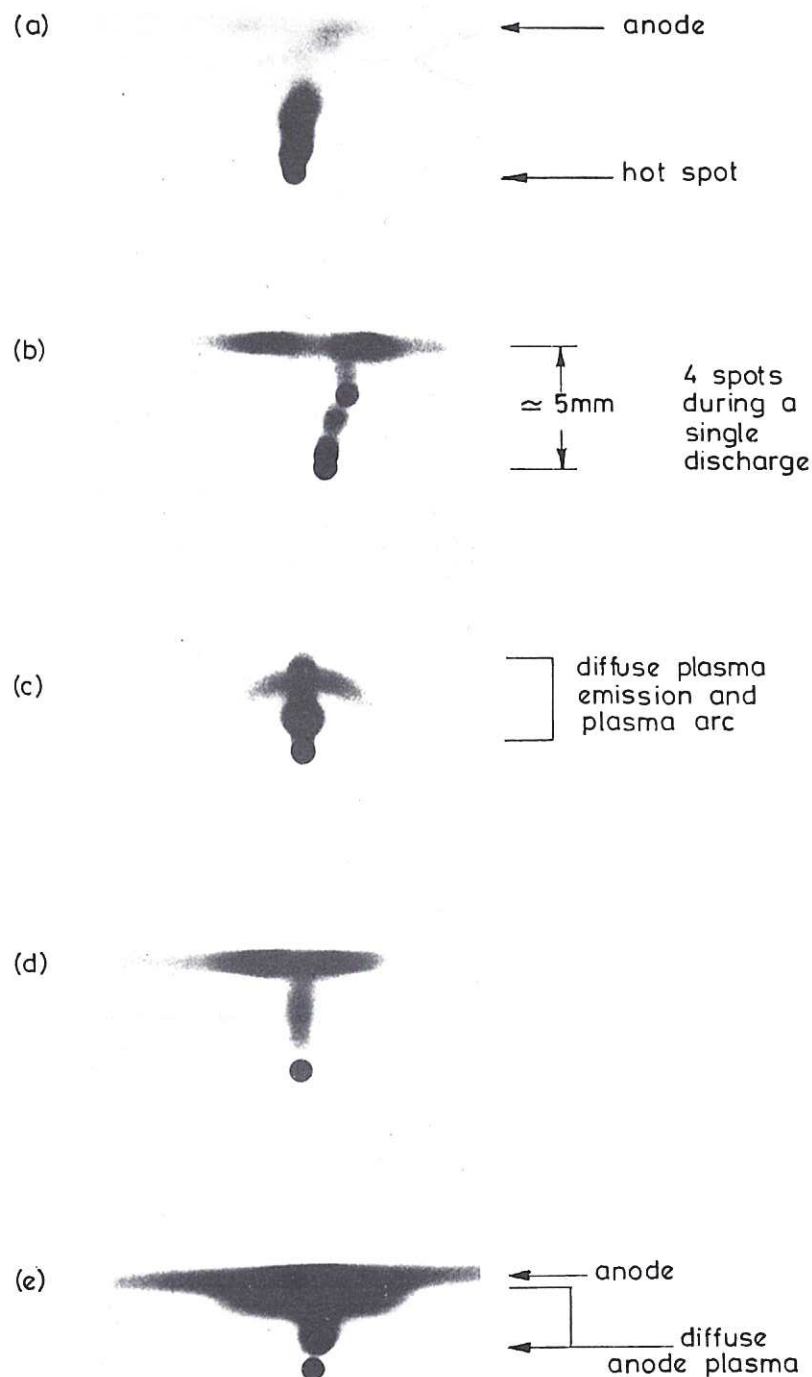


Fig.6 X-ray pin-hole photographs of the different types of 'hot-spot' formation which can occur when using the electrode configuration of Fig.2 operated with the lower as the cathode. The most intense spot occurs near the cathode surface and is on-axis. Each frame was produced by a single capacitor discharge. Frame b shows that up to 4 spots can be produced during a single discharge, and probably during the first quarter cycle of the circuit current.

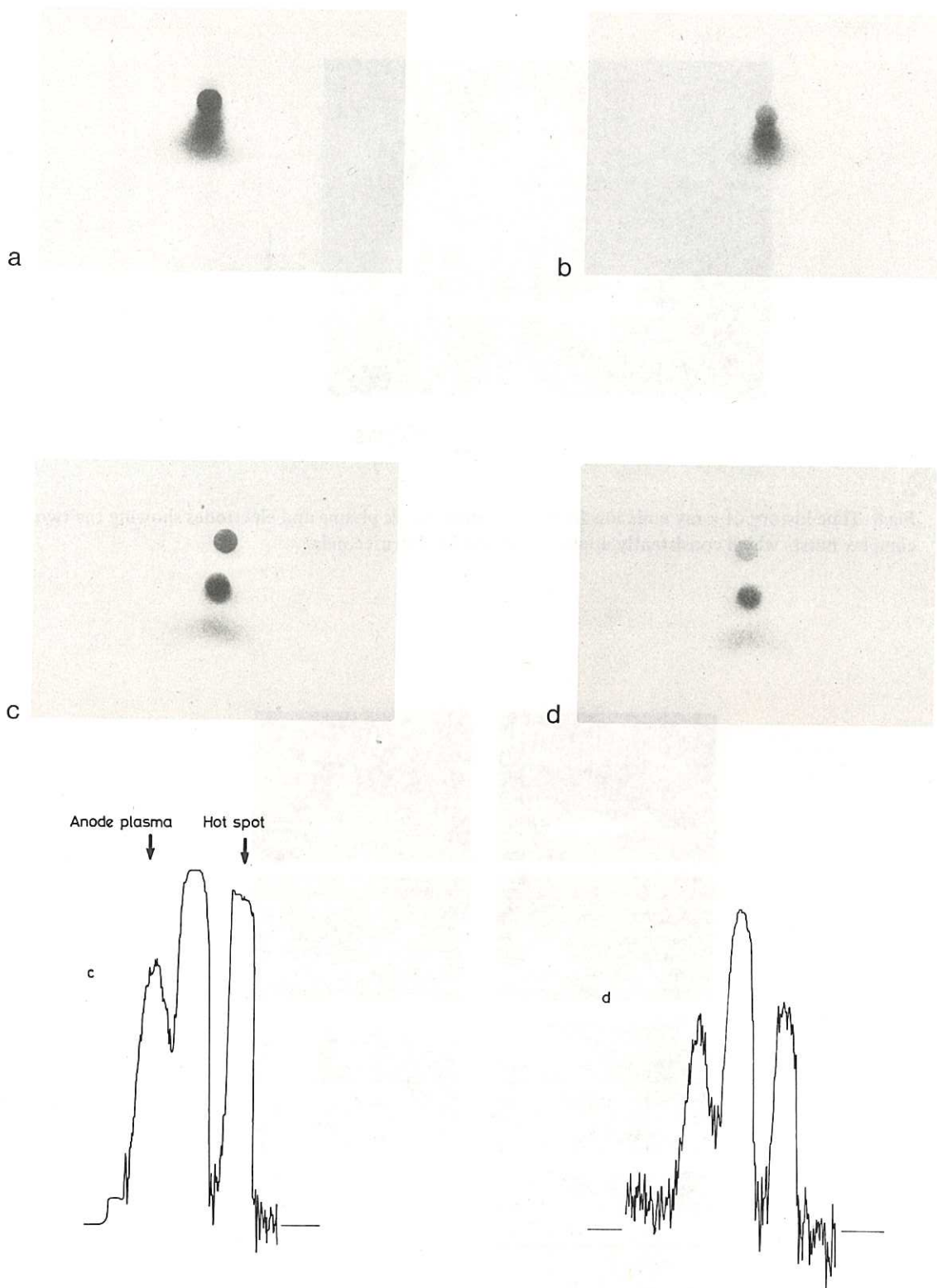


Fig.7 X-ray pin-hole photographs taken through a Ross filter system, section 4. The microphotometer traces illustrate the spatial separation of the spectral intensities from the upper most, 'hot-spot' and the lower anode plasma. The intensities of the 'hot-spots' in c and d differ by the emission from highly ionised species, mainly H-, He- and Li-like ions.

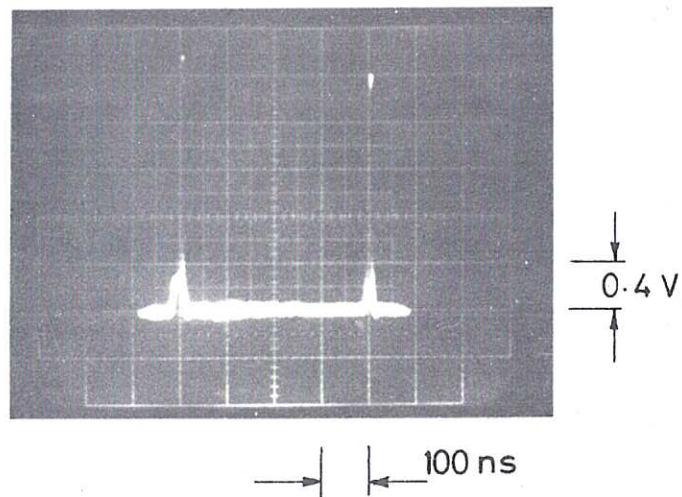


Fig.8 Time history of x-ray emission from the vacuum spark plasma and electrodes showing the two complex bursts which consistently appear separated by 400 nseconds.

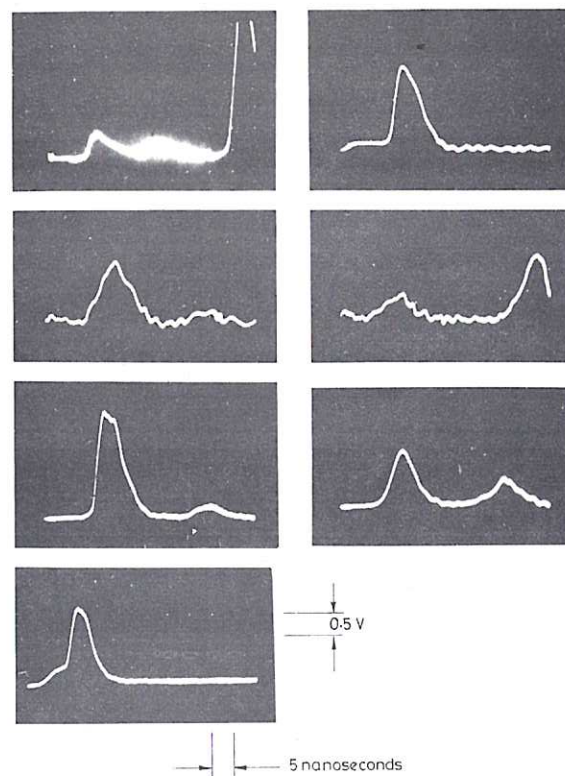


Fig.9 Life time of the 1st complex x-ray burst with spatial resolution to ensure that emission originates only in the plasma.

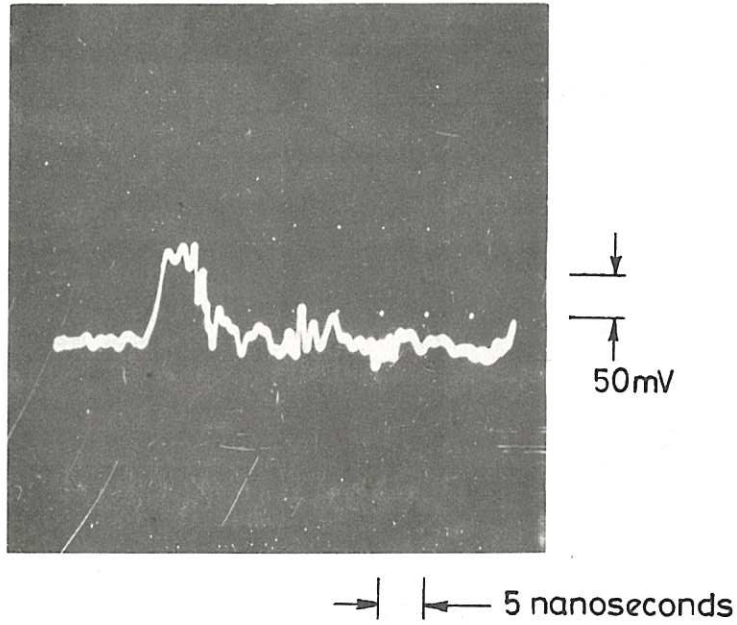


Fig.10 Probable life time measurement of the Fe XXV line emission taken with a Johansson crystal spectrometer and PIN diode.

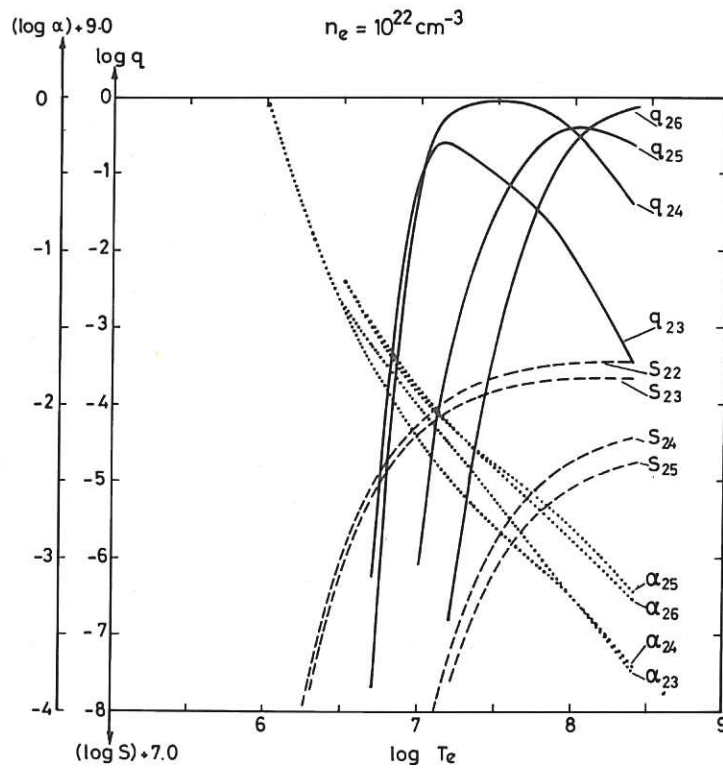


Fig.11 Ionisation rate (S), recombination rate (α) and ion population q_z as a function of temperature for a steady state iron plasma at an electron density of 10^{22} cm^{-3} .

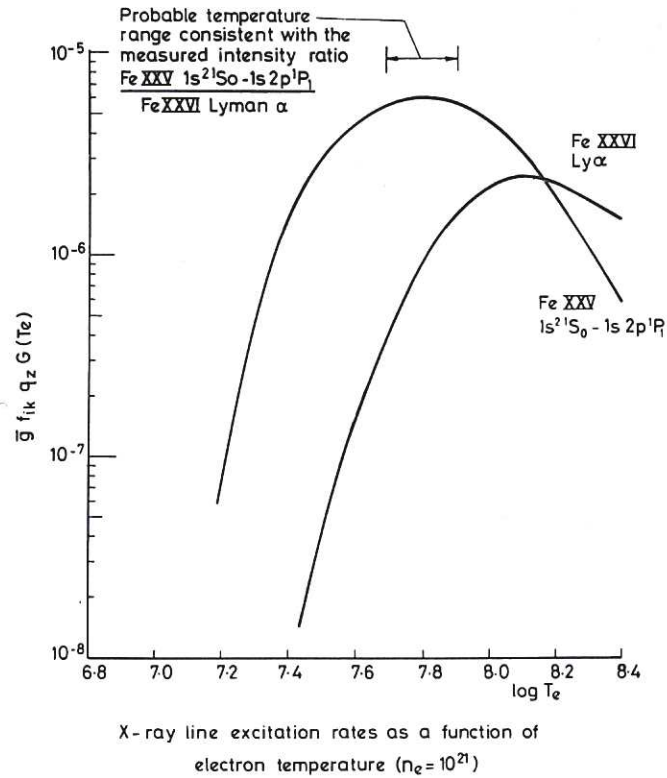


Fig.12 Excitation rate of the Fe XXV ($1s^2 1S_0 - 1s 2p^1P_1$) line at 1.85 \AA and the Fe XXVI Lyman α line at 1.78 \AA . The function shown also includes the effect of the population of each ion stage as a function of temperature q_z .

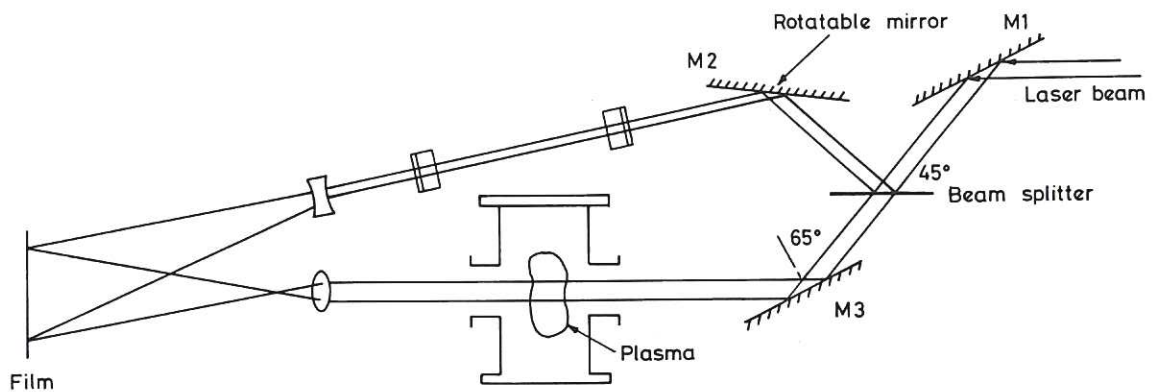
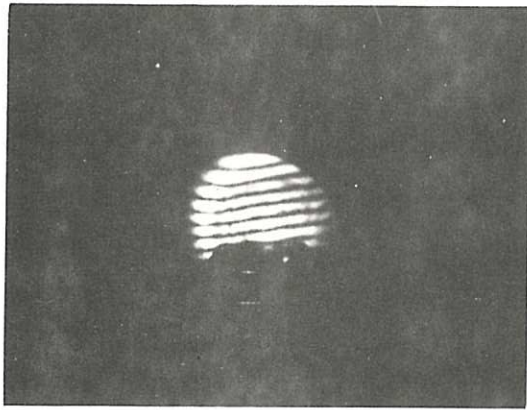


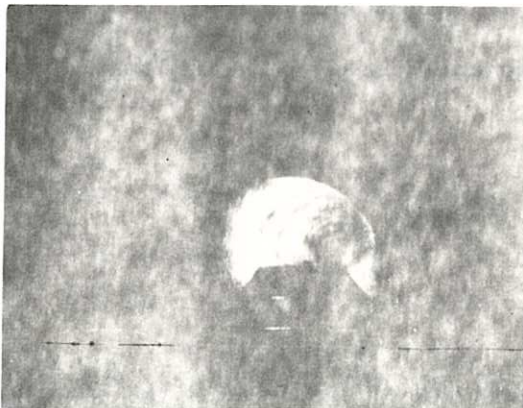
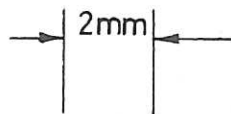
Fig.13 Lay-out of the optical components for the two-exposure microscopic holography.



$t = 0$



$t = 1 \mu s$



$t = 1.9 \mu s$



$t = 3 \mu s$

Fig.14 Reconstructed holograms at 4 different times relative to the laser pulse which triggered the vacuum spark discharge.

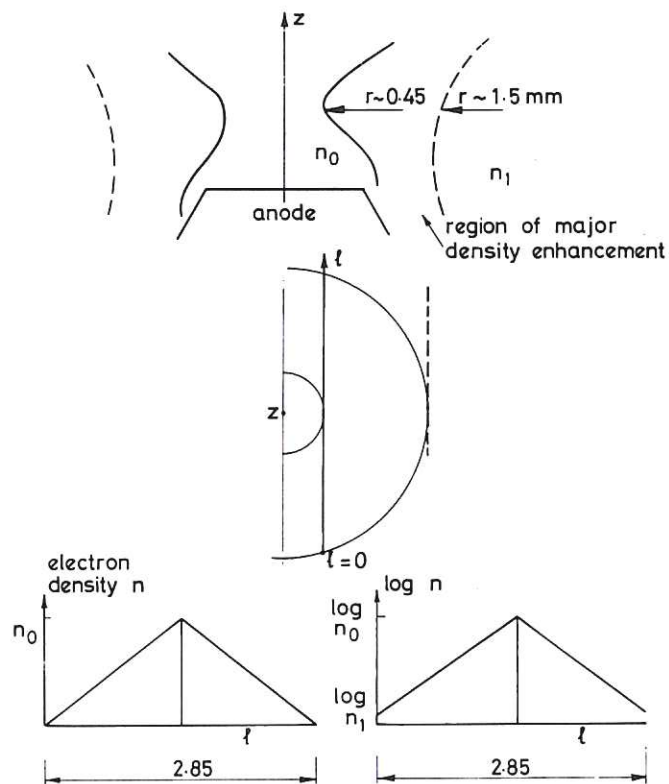


Fig.15 Simple models for deducing the average electron density n_0 (not the 'hot-spot' density) that lies within $r = 0.45$ mm of the axis of symmetry.

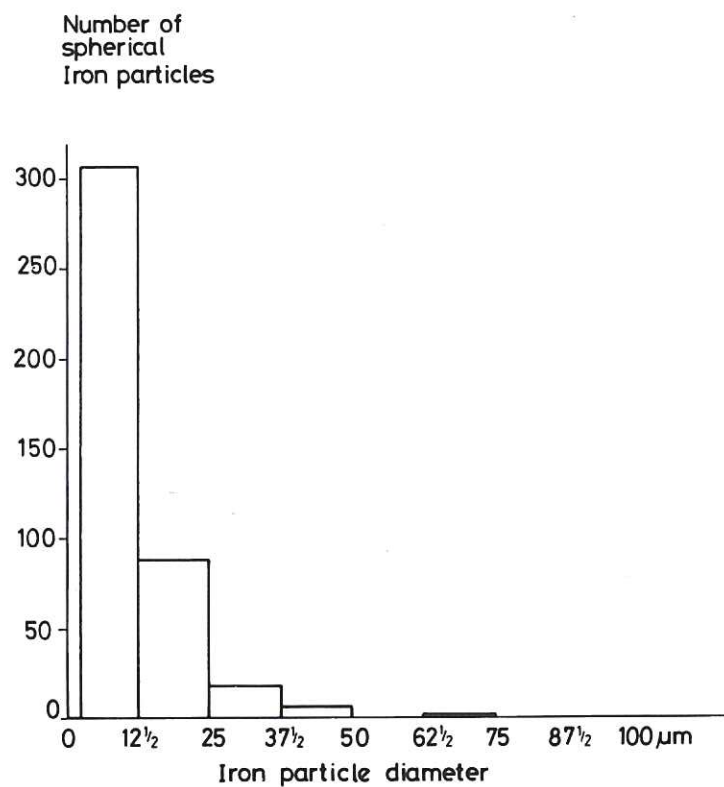


Fig.16 Distribution of iron powder size formed in the chamber after a number of plasma discharges.

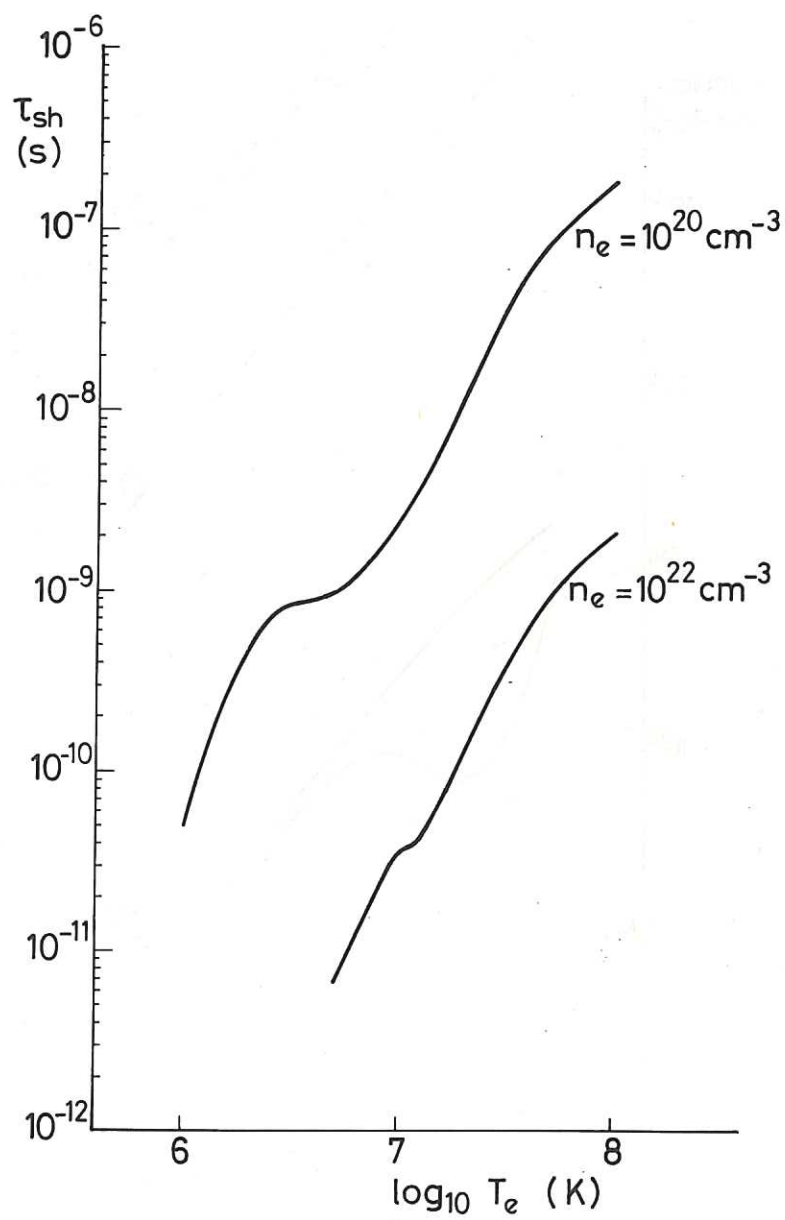


Fig.17 Isothermal shrinkage times for a cylindrical plasma column.

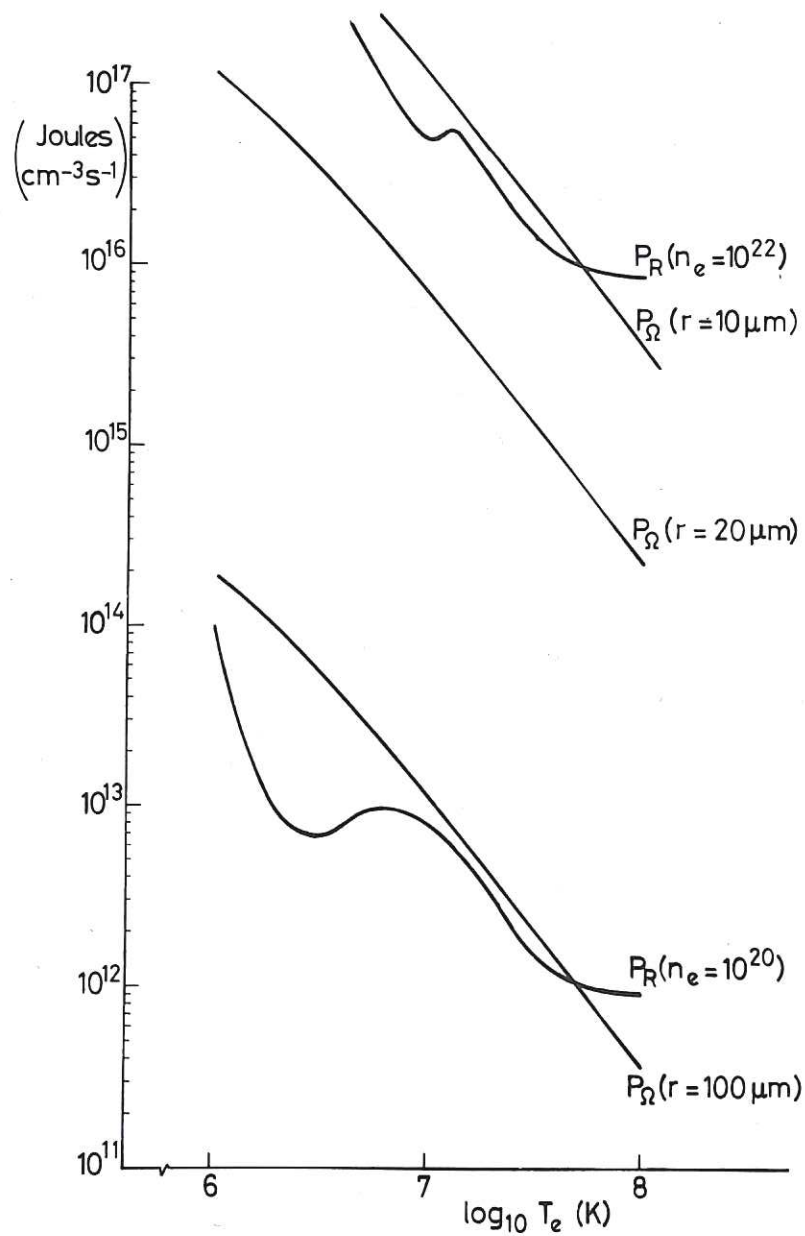


Fig.18 Ohmic heating rates (P_Ω) and relative cooling rates (P_R) based on line emission rates from all ion stages of iron. Lines included are for $\Delta n = 0$ and $\Delta n > 0$ transitions. The latter dominate for $\log T_e > 6.7$ and lie mainly in the sensitive region of our pin-hole camera.

100

100